ORIGINAL RESEARCH ARTICLE

Preparation of PbTiO₃-CdS nanocomposite material and its microstructure and photocatalytic properties

Mingdong Xu, Wenqiang Li, Shun Liu, Tao Zhang, Sen Lai, Simin Yin*

Faculty of Mechanical Engineering & Automation, Zhejiang Sci-Tech University, Hangzhou 310018, Zhejiang, China. E-mail: yinsm@zstu.edu.cn

ABSTRACT

In order to explore the influence of the ferroelectric surface on the structure and properties of semiconductor oxides, the growth of CdS nanocrystals was regulated and controlled by taking single-crystal perovskite PbTiO₃ nanosheets as the substrate through a simple hydrothermal method. Through composition design, a series of PbTiO₃-CdS nanocomposite materials with different loading concentrations were prepared, and their microstructure and photocatalytic properties were systematically analyzed. Studies show that in the prepared product, CdS nanoparticles selectively grow on the surfaces of PbTiO₃ nanosheets, and their morphology is affected by the exposed surfaces of PbTiO₃ nanosheets. There is a clear interface between the PbTiO₃ substrate and CdS nanoparticles. The concentration of the initial reactant and the time of hydrothermal reaction also significantly affect the crystal morphology of CdS. Photocatalysis studies have shown that the prepared PbTiO₃-CdS nanocomposite material has a significant degradation effect on 10 mg/L of Rhodamine B aqueous solution. The degradation efficiency rises with the increase of CdS loading concentration. When degrading 10 mg/L of Rhodamine B aqueous solution, the PbTiO₃-CdS sample with a mass fraction of 3% can reach a degradation rate of 72% within 120 min.

Keywords: CdS; Single-Crystal Perovskite; PbTiO₃; Nanocomposite Material; Photocatalysis

ARTICLE INFO

COPYRIGHT

1. Introduction

Nano materials have many characteristics, such as small size effect, surface effect, volume effect and unique photoelectric effect, which make them have broad application prospects in energy environment, electronic devices, biomedicine and so on[1–3]. Perovskite phase PbTiO₃ is a typical ferroelectric oxide material. It was reported by Shirane *et al.*[4] in 1950 that the PbTiO₃ is with a Curie temperature of about 480 ℃, and with high spontaneous polarization intensity, large dielectric constant and small dielectric loss. It is widely used in sensing, storage, infrared imaging and nano generator devices[5,6]. With the in-depth study of perovskite materials, researchers have made breakthroughs in the surface research of nanostructures of perovskite materials, and the research of the special surface ferroelectric polarization characteristics has gradually become an important direction[7]. Using the composite-preparation technology and the ferroelectric polarization characteristics on the surface of perovskite nanostructures can regulate the crystal growth of semiconductor oxides, so as to prepare new nanocomposite materials[8]. Previous studies have shown that nanocomposite materials have unique electron transport characteristics due to their special energy band structure and surface effects, so

they have become a research hotspot in the fields of solar cells, gas-phase catalysis, photocatalysis etc.[9]

In 1972, Fujishima *et al.*[10] reported the research on the photolysis of water. In this research, TiO_2 was used as a photoelectric electrode to decompose water under visible light to prepare hydrogen. Semiconductor[11] was used as an important research object of photocatalytic materials. Researchers have systematically studied other semiconductor oxide systems, such as g-C_3N_4[12,13], ZnO[14], MoS_2[15], and Fe_2O_3[16]. Among many semiconductors, CdS[17] is a promising photocatalytic material because of its small band gap ($E_g \approx 2.4$ eV) and good optical response in the visible band. However, due to its low electron-hole separation efficiency and electron mobility, CdS crystal materials prepared by traditional methods are easy to agglomerate and form large particles, resulting in a significant reduction in their specific surface area, which seriously affects the photocatalytic efficiency of CdS. In view of the above problems, existing studies mainly promote the photocatalytic efficiency of CdS by loading precious metals, such as Pt[18], Ag[19], and Au[20], etc. However, due to the rarity of precious metals and the easy oxidation of CdS, the preparation cost of photocatalytic materials increases.

In this paper, $PbTiO_3$-CdS nanocomposite materials were successfully synthesized by a secondary hydrothermal method with single-crystal perovskite phase $PbTiO_3$ nanosheets as substrates and $CdCl_2·5/2H_2O$ and CH_4N_2S as main reactants. Their microstructure and crystal growth were systematically studied. The photocatalytic properties of the prepared $PbTiO_3$-CdS nanocomposite materials were evaluated by the degradation efficiency of Rhodamine B aqueous solution under ultraviolet light and UV-Vis diffuse reflectance spectrum, which provided experimental material and theoretical basis for the subsequent exploration of the synthesis and properties of more nanocomposite materials.

2. Experiment

2.1 Experimental reagents

Potassium hydroxide (KOH, analytical pure, Hangzhou Gaojing Chemical Co., Ltd.); Titanium dioxide (P25 TiO_2, analytical pure, Shanghai Aladdin Biochemical Technology Co., Ltd.); Lead nitrate ($Pb(NO_3)_2$, analytical pure, Shanghai Zhanyun Chemical Co., Ltd.); Cadmium chloride hemihydrate ($CdCl_2·5/2H_2O$, analytical purity); Thiourea (CH_4N_2S, analytical purity) and Rhodamine B ($C_{28}H_{31}CIN_2O_3$, analytical purity) were provided by McLean Biochemical Technology Co., Ltd.; Absolute ethanol (C_2H_6O, analytical purity, Anhui Ante Food Co., Ltd.); Deionized water (H_2O, self-made in the laboratory).

2.2 Synthesis of materials

2.2.1 Preparation of single-crystal perovskite phase $PbTiO_3$ nanosheets

Single-crystal perovskite phase $PbTiO_3$ nanosheets were prepared by the method in the literature[21]. 0.4 g of TiO_2 powder was added to 6 mol/L of KOH aqueous solution to obtain a solution containing Ti^{4+} with the concentration of 0.1 mol/L. In the stirred state, 0.2 mol/L of $Pb(NO_3)_2$ aqueous solution was added to the Ti^{4+}-contained solution to adjust the ratio of lead-titanium to 2:0 and stirred for 2 h. The obtained hydroxide solution of titanium and lead was transferred to the inner tank of a 50 mL stainless steel reactor, sealed, and then hydrothermal reaction was carried out at 200 °C for 12 h. After the sample was cooled to room temperature, the sample was centrifuged and cleaned with deionized water and absolute ethanol respectively until the washing solution was neutral. Finally, the washed sample was dried at 60 °C for 24 h to obtain the $PbTiO_3$ nanosheet sample to be tested.

2.2.2 Preparation of the $PbTiO_3$-CdS nanocomposite materials

0.2 g of prepared $PbTiO_3$ nanosheets were dispersed in 30 mL of deionized water to obtain a white suspension. $CdCl_2·5/2H_2O$ and CH_4N_2S were added to the above white suspension at a molar ratio of 1:1 to obtain a mixed solution, which was continuously stirred at room temperature for 30 min. Transfer the above mixed solution to the inner tank of a 50 mL stainless steel reactor, seal it, and then conduct hydrothermal reaction at 160 °C for 12 h.

After cooled to room temperature, the sample was centrifuged and cleaned with deionized water and absolute ethanol respectively until the washing solution was neutral. Finally, the washed sample was dried at 60 °C for 24 h to obtain the target product sample to be tested.

2.2.3 Preparation of CdS crystals (contrast samples)

Using the above synthesis method, CdS crystals grown separately were prepared without adding $PbTiO_3$ nanosheets. The specific synthesis process is as follows: add $CdCl_2·5/2H_2O$ and CH_4N_2S with a molar ratio of 1:1 in 30 mL of deionized water, and obtain the precursor solution by magnetic stirring. After continuous stirring at room temperature for 30 min, transfer the above solution to the inner tank of a 50 mL stainless steel reactor for sealing, and conduct hydrothermal reaction at 160 °C for 12 h. After the reaction, cool the sample to room temperature, centrifuge and clean it with deionized water and absolute ethanol respectively until the eluent was neutral. Finally, the washed sample was dried at 60 °C for 24 h to obtain the contrast product sample to be tested.

2.3 Testing and characterization

2.3.1 Microscopic characterization of materials

The surface morphology of the material was characterized by a Zeiss ULTRA-55 scanning electron microscope (SEM), and the acceleration voltage was 5 kV.

The powder sample was added to the resin with curing agents, stirred and cured by heating. A Leica EM TRIM2 paraffin slicer was used to slice the resin embedded samples. A JEOL-200CX transmission electron microscope (TEM) was used to characterize the fine structure of the materials, and a high resolution transmission electron microscope (HRTEM) was used for imaging analysis, the acceleration voltage of was greater than or equal to 200 kV, the lattice resolution was less than 0.15 nm and the point resolution was 0.21 nm.

2.3.2 Phase analysis of materials

A Shimadzu XRD-6000 X-ray diffractor was used to carry out phase analysis of materials, with Cu K_a ($\lambda = 0.15406$ nm) as the radioactive source, with a scanning speed of 3 (°)/min and scanning range of 10.0° to 80.0°.

2.3.3 Test of photocatalytic performance

0.2 g of prepared powder sample was dispersed in 50 mL of Rhodamine B aqueous solution (10 mg/L) and dark treated for 30 min to reach adsorption equilibrium. Then, place it in a photochemical reactor (YZ-GHX-A, Shanghai Yanzheng Experimental Instrument Co., Ltd.) and degrade Rhodamine B aqueous solution under UV irradiation of 500 W mercury lamp. Under continuous stirring and illumination, take out 3 mL mixed solution every 20 min, and centrifuge at the speed of 4000 r/min for 5 min to remove the sediment. Measure the absorption peak of the separated supernatant at the wavelength of 554 nm under a UV-Vis gradiometer (UV-1800, Shanghai Mapda Instrument Co., Ltd.). In order to intuitively express the degradation efficiency of Rhodamine B aqueous solution, data processing is carried out through formula (1):

$$Degradation\ rate\ /\% = C/C_0 \times 100 \tag{1}$$

In the formula, C_0 is the initial mass concentration of Rhodamine B aqueous solution, mg/L; C is the mass concentration of the upper clear liquid at an interval, mg/L.

2.3.4 Analysis of UV-Vis diffuse reflectance absorption spectrum

A Shimadzu UV-3600 UV-VIS-NIR spectrophotometer was used for UV-Vis diffuse reflection absorption spectrum analysis. The band gap E_g of Ahv-hv image fitted by equation (2):

$$\alpha h v = c(h v - E g)^2 \tag{2}$$

In the formula, α is the absorbance coefficient, which is directly proportional to absorbance A, and it does not affect the fitting result of the band gap width E_g, so in the final image, α is replaced by A, c is a constant. hv is obtained from equation (3):

$$h v = (h \times c)/\lambda \tag{3}$$

In the formula: h is Planck constant, $h = 6.63 \times 10^{-34}$ J; c is the speed of light, taken as 3×10^8 m/s; the unit of hv is J. According to 1 eV = 1.6×10^{-19} J, the obtained hv was converted to eV.

3. Results and analysis

3.1 Analysis of the morphology of the PbTiO₃-CdS nanocomposite materials

Figure 1(a) is the SEM diagram of the perovskite phase $PbTiO_3$ sample prepared by the hydrothermal method. As can be seen from **Figure 1(a)**, the $PbTiO_3$ sample is a sheet square with a side length of about 600 nm and a thickness of about 100 nm, with smooth surface, regular morphology and good dispersion. Its large-area exposed surface is (001) crystal surface[21]. **Figure 1(b)** shows the contrast sample, that is the morphology of CdS particles grown alone without $PbTiO_3$ nanosheet substrate. According to **Figure 1(b)**, the CdS particles grown alone were of micron structure with leaf and branch morphology with size of 2–3 μm. The surface is smooth and flat, with clear particle contour and aggregation tendency. **Figures 1(c)–(e)** are SEM images of samples with different CdS loading concentrations. As can be seen from **Figure 1(c)**, most of the $PbTiO_3$ nanosheets in the sample with $PbTiO_3$-CdS mass fraction of 1% have smooth surface and no obvious adhesion of CdS nanoparticles. It can be seen from **Figure 1(d)** that more CdS nanoparticles with a size of about 10 nm are grown on the (001) crystal surface of $PbTiO_3$ nanosheets in the sample with $PbTiO_3$-CdS mass fraction of 2%. **Figure 1(e)** shows that in the sample with $PbTiO_3$-CdS mass fraction of 3%, CdS is not only dispersed on the (001) crystal plane of $PbTiO_3$, but a small amount of CdS is selectively dispersed on the side of $PbTiO_3$ nanosheets, that is, the (100) or (010) crystal plane. With the increase of CdS loading concentration, the amount of particles grown on $PbTiO_3$ nanosheets gradually increases, and its growth crystal surface has obvious selectivity, which may be related to the polarity of the exposed crystal surface of $PbTiO_3$ nanosheets. Under different initial reactant additions, it can also be observed that there is crystal plane selectivity in the growth of CdS nanoparticles on $PbTiO_3$ nanosheets, that is, it is preferred to nucleate and grow on the strongly polarized plane, and then composite on other crystal planes.

(a) PbTiO₃ nanopsheet   (b) CdS particles

(c) PbTiO₃-CdS with a mass fraction of 1%   (d) PbTiO₃-CdS with a mass fraction of 2%   (e) PbTiO₃-CdS with a mass fraction of 3%
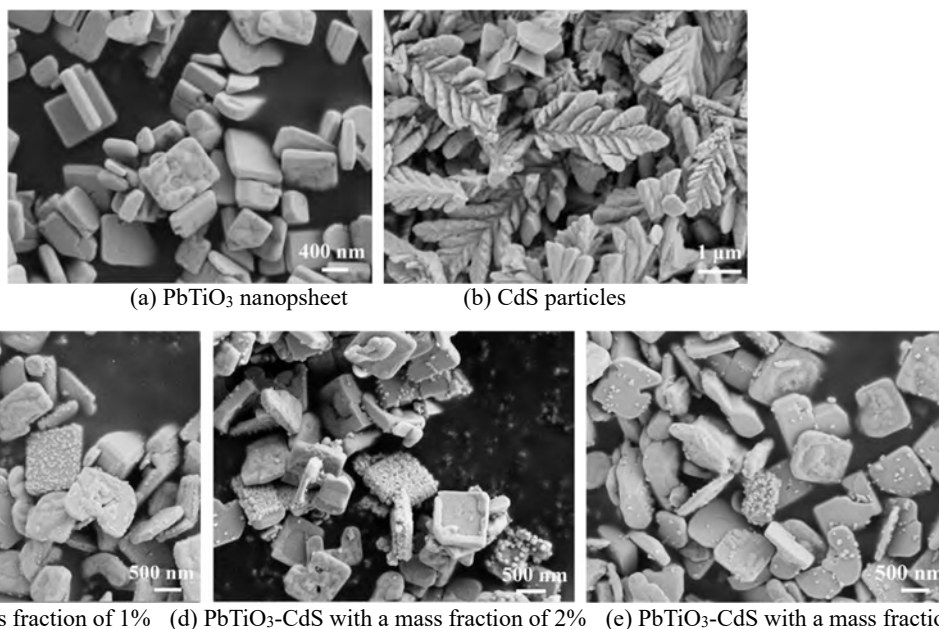
Figure 1. SEM images of single-crystal perovskite phase PbTiO₃ nanosheets synthesized by the hydrothermal method, CdS particles and PbTiO₃-CdS nanocomposite materials with different CdS loading concentrations.

3.2 Phase analysis of PbTiO₃-CdS nanocomposite materials

Figure 2(a) shows the XRD pattern of perovskite phase $PbTiO_3$ nanosheets prepared by the hydrothermal method, with all corresponding diffraction peaks (JCPDS: 06-0452), sharp diffraction peaks, good crystallinity and no impurity diffraction peaks. The diffraction peak intensity of its (001) crystal plane is almost equal to the highest peak

(101) of the standard diffraction pattern, indicating that the prepared $PbTiO_3$ sample has a large number of (001) exposed surface, which is consistent with the observation results reported in the literature[21] and **Figure 1(a)**. **Figure 2(b)** shows the XRD patterns of CdS particles grown alone and samples with different CdS loading concentrations. It can be seen from the figure that the diffraction peaks of CdS particle samples synthesized separately all correspond to the standard PDF card (JCPDS: 41-1049), with sharp diffraction peaks and no impurity diffraction peaks. The diffraction peaks of $PbTiO_3$-CdS with a mass fraction of 1%, 2% and 3%

are obvious, and the diffraction of $PbTiO_3$ is more intense, and the diffraction peak of CdS is relatively weak. With the increase of CdS loading concentration, the diffraction peak is gradually obvious. It is consistent with the SEM results in **Figures 1(c)** to **(e)**. And in the XRD diffraction pattern of $PbTiO_3$-CdS nanocomposite materials, the diffraction peak intensity corresponding to the (001) crystal plane in $PbTiO_3$ (JCPDS: 06-0452) decreases, which may be related to the selective growth of CdS on the (001) crystal plane of $PbTiO_3$ nanosheets.

(a) $PbTiO_3$ nanosheets   (b) Single-synthesized CdS particles
$PbTiO_3$-CdS with a mass fraction of 1%, 2%, 3%
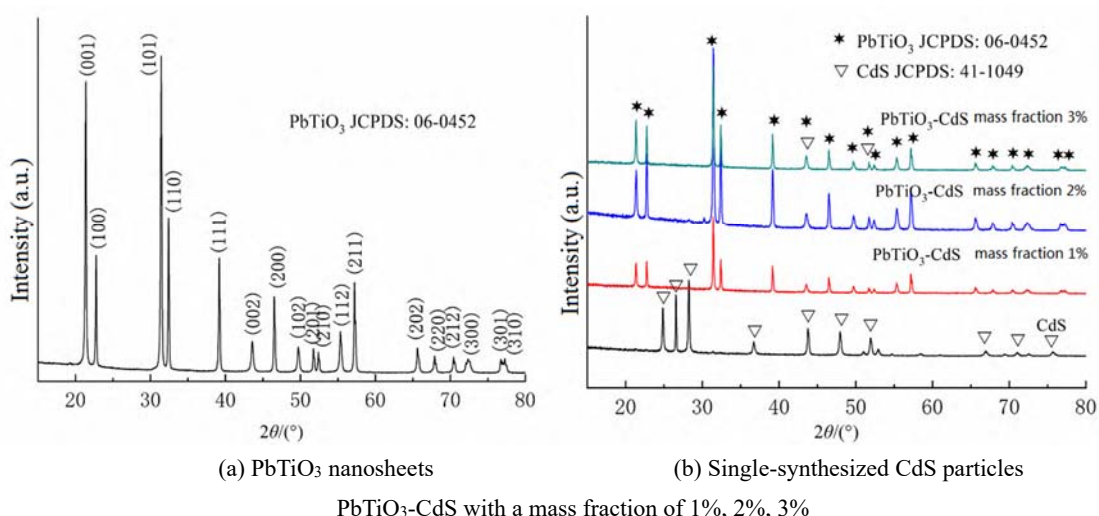
Figure 2. XRD patterns of single-crystal perovskite phase $PbTiO_3$ nanosheets synthesized by the hydrothermal method, single-synthesized CdS particles and $PbTiO_3$ CdS nanocomposite materials with different CdS loading concentrations.

3.3 Microstructure analysis of PbTiO₃-CdS nanocomposite materials

In order to further explore the growth and morphology of CdS nanoparticles on the surface of perovskite $PbTiO_3$ nanosheets, the resin embedded sections of $PbTiO_3$-CdS nanocomposite materials were characterized and analyzed by TEM and HRTEM. As shown in **Figure 3(a)**, CdS nanoparticles are dispersed on the upper and lower crystal planes of $PbTiO_3$ nanosheets, and an obvious lattice interface is formed, as shown in **Figure 3(b)**. The

nanoparticle has complete outline and clear lattice, and its crystal plane spacing is 0.316 nm and 0.245 nm respectively, which corresponds to the (101) and (102) crystal planes of CdS (JCPDS: 41-1049). The crystal plane spacing of $PbTiO_3$ nanosheets is 0.415 nm and 0.390 nm respectively, which corresponds to the (001) and (100) crystal planes of $PbTiO_3$ (JCPDS: 06-0452). Therefore, it is further proved that the prepared samples are $PbTiO_3$-CdS nanocomposite materials, and CdS nanoparticles grow selectively on the surface of $PbTiO_3$ nanosheets.

(a) TEM (b) HRTEM
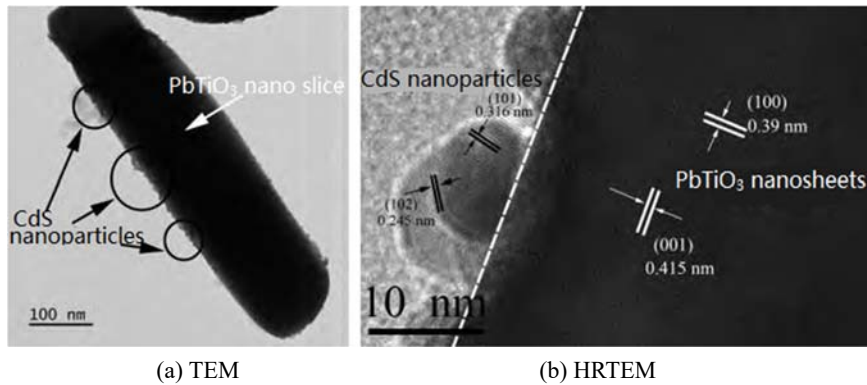
Figure 3. TEM and HRTEM diagrams of PbTiO$_3$-CdS nanocomposite materials synthesized by the hydrothermal method.

3.4 Growth process of PbTiO$_3$-CdS nanocomposite materials

In order to further explore the growth process of PbTiO$_3$-CdS nanocomposites, PbTiO$_3$-CdS nanocomposite materials grown under different hydrothermal reaction time were analyzed. **Figure 4** and **Figure 5** show the SEM and XRD results of the prepared samples respectively. As can be seen from **Figure 4**: (a) no obvious CdS nanoparticles were observed on the surface of PbTiO$_3$ nanosheets in the 0.5-h sample, and there was no corresponding diffraction peak in XRD. At this time, CdS had not crystallized because the hydrothermal time was too short. (b) Fine CdS nanoparticles with a size of about 10 nm have appeared on the surface of PbTiO$_3$ nanosheets in the 3-h sample. Comparing the XRD pattern of this sample with that of the 0.5-h sample, it can be found that the diffraction peak corresponding to CdS gradually strengthen. (c) The CdS nanoparticles grown on the surface of PbTiO$_3$ nanosheets in the 5-h sample gradually increased, and grew on each surface. Compared with the XRD pattern of 3-h sample in (b), the diffraction peak corresponding to CdS in this sample pattern was enhanced again. With the extension of the reaction time to 7 h in (d), the size and quantity of CdS nanoparticles on the surface of PbTiO$_3$ nanosheets increase. At this time, CdS nanoparticles can be obviously observed on some surfaces of PbTiO$_3$ nanosheets, with smooth surfaces and no

particle adhesion. Therefore, it can be seen that the growth of CdS on the surface of PbTiO$_3$ nanosheets appears selectivity under the growth conditions. With the further extension of the reaction time (**Figures 4(e)–(f)**), the size of CdS nanoparticles on the surface of PbTiO$_3$ nanosheets remains stable, and its growth selectivity is more obvious. Statistically, a large number of blank exposed crystal surfaces can be observed, while a large number of CdS particles grow on other crystal surfaces. **Figure 5** shows the XRD diffraction results of the prepared samples. It can be seen from the figure that the reaction products have sharp diffraction peaks, which can correspond to two substances of perovskite phase PbTiO$_3$ (JCPDS: 06-0452) and CdS (JCPDS: 41-1049) on the standard PDF card. The diffraction results show that both PbTiO$_3$ substrate and CdS grown on its surface have good crystallinity. According to the above analysis results, with the extension of the reaction time, the growth of CdS nanoparticles on PbTiO$_3$ nanosheets was significantly regulated. CdS nanoparticles selectively grow on a crystal surface of PbTiO$_3$ nanosheets. With the increase of the hydrothermal time, according to the crystallization thermodynamics, the size of CdS nanoparticles gradually increases and stabilizes. The growth of CdS on the surface of PbTiO$_3$ nanosheets is a process regulated by thermodynamics and exposed crystal surface of PbTiO$_3$.

(a) 0.5 h   (b) 3 h   (c) 5 h

(d) 7 h   (e) 9 h   (f) 12 h
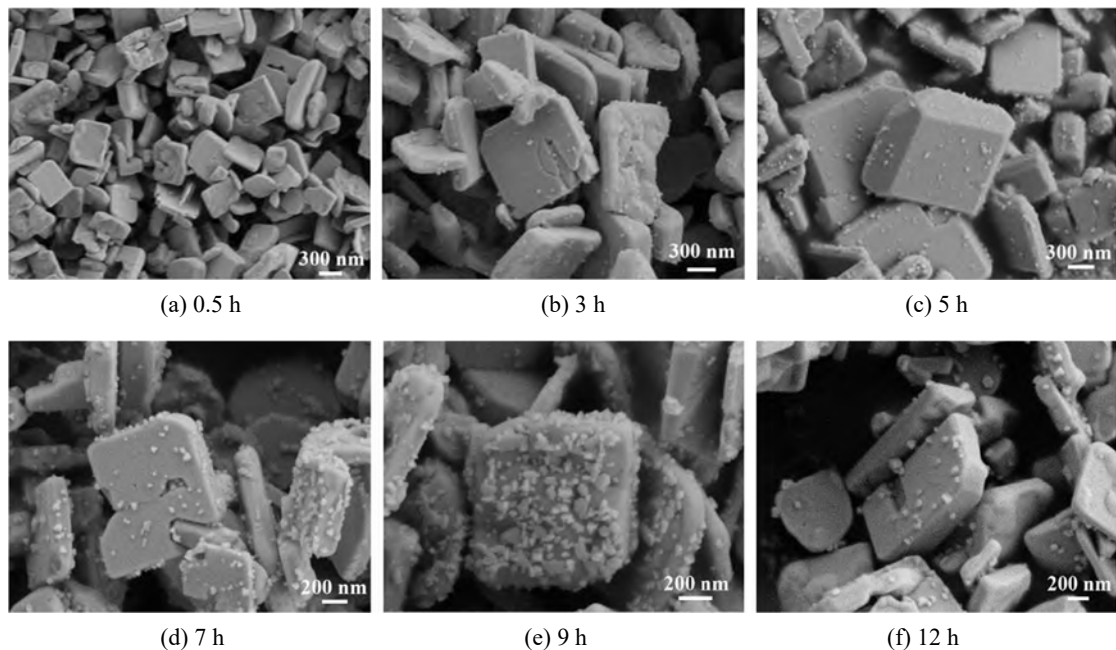
Figure 4. SEM of PbTiO$_3$-CDs nanocomposite materials synthesized under different hydrothermal reaction time.
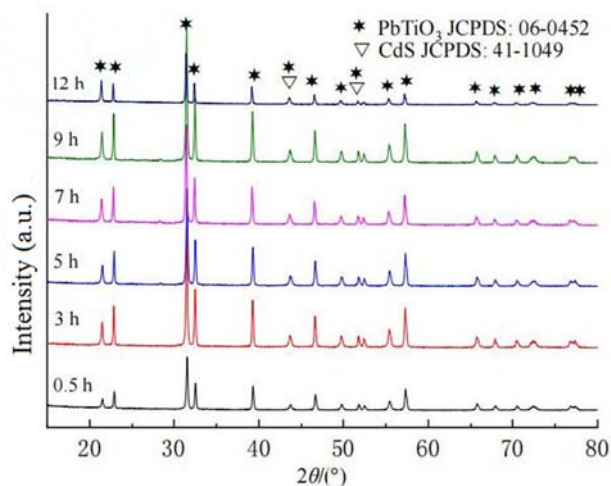
Figure 5. XRD patterns of PbTiO$_3$-CdS nanocomposite materials synthesized under different hydrothermal reaction time.

3.5 Study on the photocatalytic properties of PbTiO$_3$-CdS nanocomposite materials

Based on the above research, the photocatalytic degradation properties of the prepared PbTiO$_3$-CdS nanocomposite materials were studied. **Figure 6** shows the efficiency curves of self-degradation of Rhodamine B solution and degradation Rhodamine B solution by different samples under UV irradiation. As shown in **Figure 6,** Rhodamine B solution has slight self-degradation within 120 min, and the degradation rate is 10%, which is caused by the slight increase of the temperature of the stirred solution under UV irradiation in the experiment. PbTiO$_3$ nanosheets and PbTiO$_3$ nanosheets + CdS particles have almost the same degradation ability to Rhodamine B solution, and the degradation efficiency is low, which is 40%. It shows that the photocatalytic activity of PbTiO$_3$ nanoparticles and CdS particles is not high. The Rhodamine B solution was significantly degraded by PbTiO$_3$-CdS with a mass fraction of 1%, 2% and 3% under UV light, and the degradation rates were 60%, 64% and 72% respectively. The above results show that with the increase of CdS loading, the catalytic degradation efficiency of PbTiO$_3$-CdS nanocomposite materials on Rhodamine B aqueous solution increases significantly. The degradation efficiency of PbTiO$_3$-CdS with a mass fraction of 3% is 1.8 times higher than that of PbTiO$_3$ nanosheets and PbTiO$_3$ nanosheets + CdS particles.

25
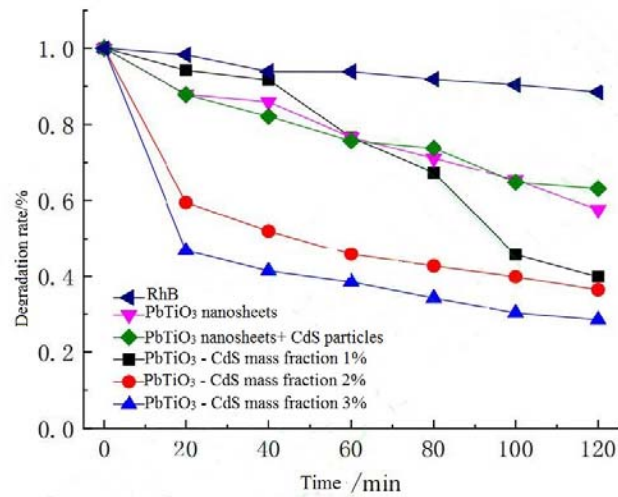
Figure 6. Efficiency curves of self-degradation of Rhodamine B solution and degradation by different samples.
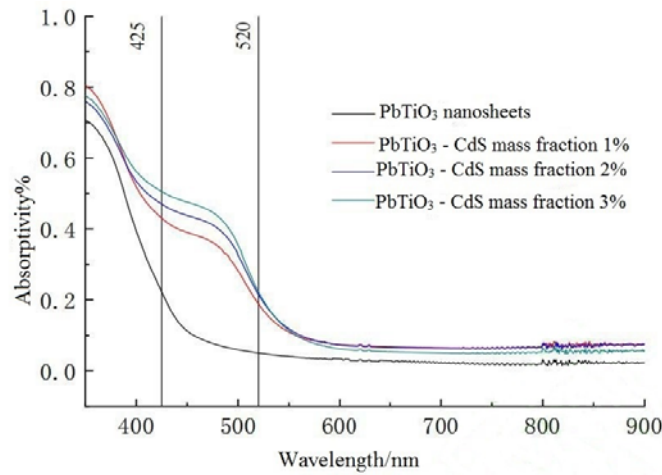
Figure 7. UV-Vis diffuse reflection absorption spectrum.
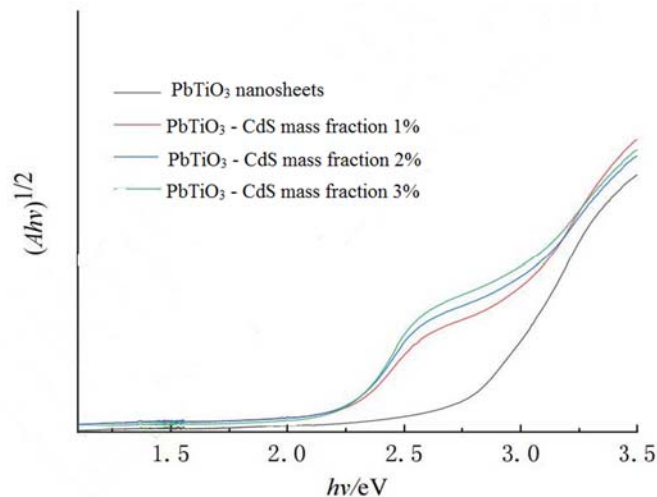
Figure 8. *Ahv-hv* fitting image.

Figure 7 shows the UV-Vis diffuse reflectance spectra of different samples. It can be seen from the figure that the prepared PbTiO$_3$-CdS nanocomposite materials have obvious absorption peaks between 425 nm and 520 nm, indicating that PbTiO$_3$-CdS nanocomposite materials have good response to visible light. With the increase of CdS loading concentration, the response of PbTiO$_3$-CdS nanocomposite materials to visible light increased slightly. The *Ahv-hv* fitting image of each sample is fitted

26

according to formula (2), as shown in **Figure 8**, and the band gap width of each sample is shown in **Table 1**. The two band gap widths of PbTiO$_3$-CdS nanocomposite materials not only improve the band gap width of PbTiO$_3$ nanosheets, but also improve the band gap width of CdS particles ($E_g \approx 2.4$ eV), so as to reduce the energy required for electronic transition and improve the photocatalytic performance. With the increase of CdS loading concentration to 3%, the light absorption of PbTiO$_3$-CdS composite samples with a mass fraction of 3% in 425–520 nm band increases significantly. The increase of light absorption is conducive to the formation of electrons and holes in the composites. The absorption edge of PbTiO$_3$-CdS composite samples with a mass fraction of 3% also has a small amount of red shift, indicating that the band gap of the sample is also reduced accordingly, which is conducive to the absorption of small energy photons, promoting the generation and separation of electrons and holes, and further improving the photocatalytic performance of the sample. This is also consistent with the fact that PbTiO$_3$-CdS samples with a mass fraction of 3% show the highest photocatalytic activity on Rhodamine B aqueous solution under light. Based on the above analysis, a possible photocatalytic mechanism is proposed: perovskite PbTiO$_3$ nanosheets and CdS are used as light absorption centers to absorb photon energy and produce photogenerated carriers respectively. The CdS surface is the photocatalytic reaction center. The built-in electric field formed by the spontaneous polarization of PbTiO$_3$ nanosheets promotes the separation of electrons and holes, and the electrons are further transferred to the CdS surface for photocatalytic reaction, so as to improve the photocatalytic effect of PbTiO$_3$-CdS.

Table 1. Band gap width of PbTiO$_3$ nanosheets and PbTiO$_3$-CdS with different loading concentrations

Samples	Band gap width 1/eV	Band gap width 2/eV
PbTiO$_3$ nanosheets		2.76
PbTiO$_3$-CdS with a mass fraction of 1%	2.24	2.67
PbTiO$_3$-CdS with a mass fraction of 2%	2.21	2.52
PbTiO$_3$-CdS with a mass fraction of 3%	2.21	2.46

4. Conclusion

In this paper, PbTiO$_3$-CdS nanocomposite materials were successfully prepared by the hydrothermal method, and their microstructure and crystal growth process were systematically characterized and analyzed. On this basis, the photocatalytic properties of the prepared PbTiO$_3$-CdS nanocomposite materials were evaluated. The main conclusions are as follows:

a) The prepared PbTiO$_3$-CdS nanocomposite materials have regular morphology and good dispersion; CdS nanoparticles (about 10 nm in size) were selectively grown on the surface of perovskite PbTiO$_3$ nanosheets with good crystallinity. Compared with CdS particles with independent nucleation and crystallization, its size decreases sharply, and an obvious interface is formed with PbTiO$_3$ nanosheets. The crystal growth of PbTiO$_3$-CdS nanocomposite materials is a process regulated by the exposed crystal surface of PbTiO$_3$.

b) Hydrothermal reaction time is an important thermodynamic condition that strongly affects the crystal growth process of PbTiO$_3$-CdS nanocomposite materials. With the increase of time, the more sufficient the nucleation and crystal growth of CdS nanoparticles on the surface of PbTiO$_3$ nanosheets, the larger the CdS grain size.

c) The prepared PbTiO$_3$-CdS nanocomposite materials can degrade 10 mg/L Rhodamine B solution. With the increase of the mass fraction of PbTiO$_3$-CdS, the photocatalytic degradation efficiency of PbTiO$_3$-CdS nanocomposite materials increases. The degradation rate of PbTiO$_3$-CdS nanocomposite materials with a mass fraction of 3% was the highest at 120 min, reaching 72%.

Conflict of interest

The authors declare that they have no conflict of interest.

Acknowledgements

References

1. Niu S, Peng K, Kou J. Introduction to the photoelectric materials of nanostructure．Journal of Liaoning Normal University (Natural Science Edition) 2003; 26(1): 63–67.

2. Cao J, Wu B, Peng J, *et al*. Copper-copper iodide hybrid nanostructure as hole transport material for efficient and stable inverted perovskite solar cells. Science China Chemistry 2019; 62(3): 363–369.

3. Zhang M, Chen H, Yang X, *et al*. The development and prospect of nanometer materials. Missiles and Space Vehicles 2000; (3): 11–16.

4. Shirane G, Hoshino S, Suzuki K. X-ray study of the phase transition in lead titanate. Physical Review 1950; 80(6): 1105.

5. Yin S. Study on the surface, interface and properties of single-crystal nanostructures of perovskite ferroelectric oxide [PhD thesis]. Hangzhou: Zhejiang University; 2015. p. 35–46．

6. Qiu C, Wang B, Zhang N, *et al*. Transparent ferroelectric crystals with ultrahigh piezoelectricity. Nature 2020; 577(7790): 350–354.

7. Jiang S. Study on preparation, microstructure and applications of perovskite oxide ferroelectric nanocomposite materials [PhD thesis]. Hangzhou: Zhejiang University; 2016. p. 68–87.

8. Li X, Qiu T, Zhang J, *et al*. Terahertz field-induced ferroelectricity in quantum paraelectric $SrTiO_3$. Science 2019; 364(6445): 1079–1082.

9. Zhang M, Wang K, Du Y, *et al.* High and temperature-insensitive piezoelectric strain in alkali niobate lead-free perovskite. Journal of the American Chemical Society 2017; 139(10): 3889–3895.

10. Fujishima A, Honda K. Electrochemical photolysis of water at a semiconductor electrode. Nature 1972; 238(5358): 37–38.

11. Molaei MJ. The optical properties and solar energy conversion applications of carbon quantum dots: A review. Solar Energy 2020; 196: 549–566.

12. Feng Z, Zeng L, Zhang Q, *et al*. In situ preparation of g-C_3N_4/$Bi_4O_5I_2$ complex and its elevated photoactivity in Methyl Orange degradation under visible light. Journal of Environmental Sciences 2020; 87: 149–162.

13. Wang T, Nie C, Ao Z, *et al*. Recent progress in g-C_3N_4 quantum dots: Synthesis, properties and applications in photocatalytic degradation of organic pollutants. Journal of Materials Chemistry A 2020; 8(2): 485–502.

14. Jamil A, Bokhari TH, Javed T, *et al*. Photocatalytic degradation of disperse dye Violet-26 using TiO_2 and ZnO nanomaterials and process variable optimization. Journal of Materials Research and Technology 2020; 9(1): 1119–1128.

15. Ghasemipour P, Fattahi M, Rasekh B, *et al*. Developing the ternary ZnO doped MoS_2 nanostructures grafted on CNT and Reduced Graphene Oxide (RGO) for photocatalytic degradation of aniline. Scientific Reports 2020; 10: 4414.

16. Ren L, Zhou W, Sun B, *et al*. Defects-engineering of magnetic γ-Fe_2O_3 ultrathin nanosheets/mesoporous black TiO_2 hollow sphere heterojunctions for efficient charge separation and the solar-driven photocatalytic mechanism of tetracycline degradation. Applied Catalysis B: Environmental 2019; 240: 319–328.

17. Deng F, Lu X, Luo Y, *et al*. Novel visible-light-driven direct Z-scheme CdS/$CuInS_2$ nanoplates for excellent photocatalytic degradation performance and highly-efficient Cr (Ⅵ) reduction. Chemical Engineering Journal 2019; 361: 1451–1461.

18. Yang J, Yan H, Wang X, *et al*. Roles of cocatalysts in Pt-PdS/CdS with exceptionally high quantum efficiency for photocatalytic hydrogen production. Journal of Catalysis 2012; 290: 151–157.

19. Gao D, Liu W, Xu Y, *et al*. Core-shell Ag@Ni cocatalyst on the TiO_2 photocatalyst: One-step photoinduced deposition and its improved H-2-evolution activity. Applied Catalysis B: Envi-

ronmental 2020; 260: 118190.

20. Li J, Cushing SK, Zheng P, *et al*. Solar hydrogen generation by a CdS-Au-TiO$_2$ sandwich nanorod array enhanced with Au nanoparticle as electron relay and plasmonic photosensitizer. Journal of the American Chemical Society 2014; 136(23): 8438–8449.

21. Chao C, Ren Z, Zhu Y, *et al*. Self-templated synthesis of single-crystal and single-domain ferroelectric nanoplates. Angewandte Chemie International Edition 2012; 51(37): 9283–9287.

22. Zhong W, Tu W, Feng S, *et al*. Photocatalytic H$_2$ evolution on CdS nanoparticles by loading FeSe nanorods as co-catalyst under visible light irradiation. Journal of Alloys and Compounds 2019; 772: 669–674.

23. Ye K, Li Y, Yang H, *et al*. An ultrathin carbon layer activated CeO$_2$ heterojunction nanorods for photocatalytic degradation of organic pollutants. Applied Catalysis B: Environmental 2019; 259: 118085.

24. Huang X, Lei R, Yuan J, *et al*. Insight into the piezo-photo coupling effect of PbTiO$_3$/CdS composites for piezo-photocatalytic hydrogen production. Applied Catalysis B: Environmental 2021; 282: 119586.

25. Raza N, Raza W, Gul H, *et al*. Solar-light-active silver phosphate/titanium dioxide/silica heterostructures for photocatalytic removal of organic dye. Journal of Cleaner Production 2020; 254: 120031.

26. Jiang S, Ren Z, Li M, *et al*. Single-crystal heterostructured PbTiO$_3$/CdS nanorods with enhanced visible-light-driven photocatalytic performance. RSC Advances 2015; 5(67): 54454–54459.